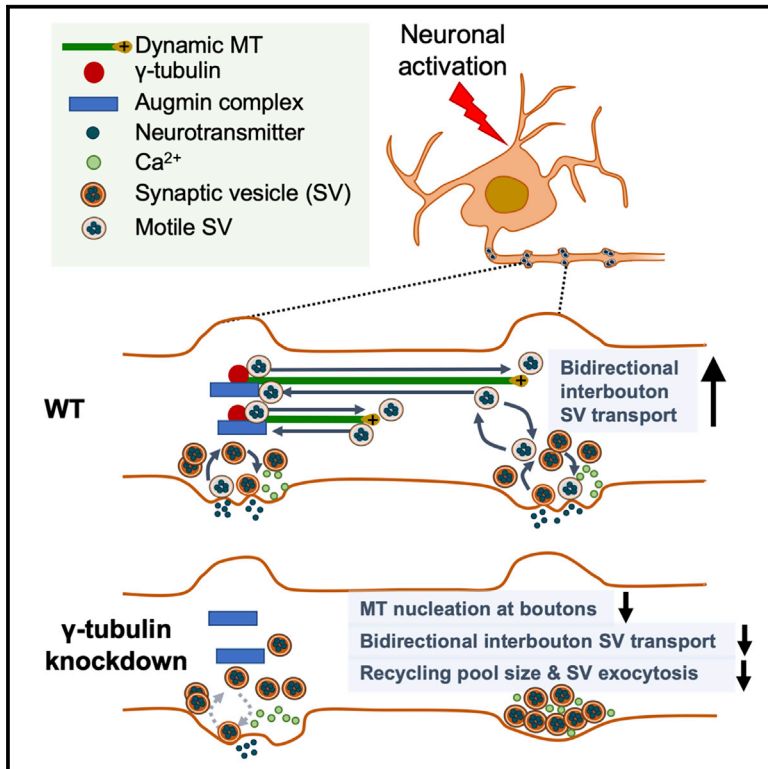


# Activity-Dependent Nucleation of Dynamic Microtubules at Presynaptic Boutons Controls Neurotransmission

## Graphical Abstract



## Authors

Xiaoyi Qu, Atul Kumar, Heike Blockus, Clarissa Waites, Francesca Bartolini

## Correspondence

fb2131@columbia.edu

## In Brief

Qu et al. demonstrate that excitatory *en passant* boutons are hotspots for neuronal activity-induced  $\gamma$ -tubulin- and augmin-dependent oriented MT nucleation and that the resulting presynaptic *de novo* nucleated MTs promote inter-bouton SV motility, which is rate limiting for neurotransmitter release.

## Highlights

- Excitatory boutons are hotspots for activity-induced MT nucleation
- Presynaptic *de novo* MT nucleation depends on  $\gamma$ -tubulin and the augmin complex
- The augmin complex is required for correct polarity of presynaptic nucleated MTs
- Presynaptic MT nucleation promotes SV motility and exocytosis at sites of release



# Activity-Dependent Nucleation of Dynamic Microtubules at Presynaptic Boutons Controls Neurotransmission

Xiaoyi Qu,<sup>1,3</sup> Atul Kumar,<sup>1</sup> Heike Blockus,<sup>2</sup> Clarissa Waites,<sup>1</sup> and Francesca Bartolini<sup>1,4,\*</sup>

<sup>1</sup>Department of Pathology & Cell Biology, Columbia University Medical Center, 630 W. 168<sup>th</sup> Street, New York, NY 10032, USA

<sup>2</sup>Department of Neuroscience, Columbia University, 3227 Broadway, New York, NY 10027, USA

<sup>3</sup>Present address: Department of Neuroscience, Genentech, Inc., 340 Point San Bruno Boulevard, South San Francisco, CA 94080, USA

<sup>4</sup>Lead Contact

\*Correspondence: fb2131@columbia.edu

<https://doi.org/10.1016/j.cub.2019.10.049>

## SUMMARY

Control of microtubule (MT) nucleation and dynamics is critical for neuronal function. Whether MT nucleation is regulated at presynaptic boutons and influences overall presynaptic activity remains unknown. By visualizing MT plus-end dynamics at individual excitatory *en passant* boutons in axons of cultured hippocampal neurons and in hippocampal slices expressing EB3-EGFP and vGlut1-mCherry, we found that dynamic MTs preferentially grow from presynaptic boutons, show biased directionality in that they are almost always oriented toward the distal tip of the axon, and can be induced by neuronal activity. Silencing of  $\gamma$ -tubulin expression reduced presynaptic MT nucleation, and depletion of either HAUS1 or HAUS7-augmin subunits increased the percentage of retrograde comets initiated at boutons, indicating that  $\gamma$ -tubulin and augmin are required for activity-dependent *de novo* nucleation of uniformly distally oriented dynamic MTs. We analyzed the dynamics of a wide range of axonal organelles as well as synaptic vesicles (SVs) relative to vGlut1<sup>+</sup> stable presynaptic boutons in a time window during which MT nucleation at boutons is promoted upon induction of neuronal activity, and we found that  $\gamma$ -tubulin-dependent presynaptic MT nucleation controls bidirectional (SV) interbouton transport and regulates evoked SV exocytosis. Hence, *en passant* boutons act as hotspots for activity-dependent *de novo* MT nucleation, which controls neurotransmission by providing dynamic tracks for bidirectional delivery of SVs between sites of neurotransmitter release.

## INTRODUCTION

Dynamic microtubules (MTs) play a crucial role for rapid forms of axonal and dendritic transport and synaptic transmission [1–3]. At postsynaptic sites, MT invasion into spines regulates spine

morphology, motor and cargo pair transport into spines, and synaptic activity [4–9].

MT dynamics and organization at presynaptic boutons, however, remains a largely uncharted area due to the limited size of the boutons in most mammalian neurons and loss of dynamic MTs using standard fixation procedures. Classic electron microscopy studies have described the presence of pools of MTs at presynaptic sites in the rat cortex and cerebellum, including synaptic vesicle (SV)-clothed MTs attached to the active zone and peripheral coils of MTs in close contact with presynaptic mitochondria [10–16]. These observations suggested that presynaptic MTs may be functionally coupled with synaptic transmission by (1) driving the interbouton translocation of SVs, (2) maintaining the composition and organization of the presynaptic active zone (AZ), (3) contributing to the maturation of postsynaptic receptors by conveying new SVs to be released at certain presynaptic sites [17], and (4) anchoring mitochondria at sites of release [14, 18]. Few studies, however, have explored these possibilities using modern imaging approaches. Presynaptic MAP-associated stable MT loops, EB1-labeled dynamic pioneer MTs, and DAAM-dependent stable MT regulation of SV release and AZ morphology have been described at the *Drosophila* neuromuscular junction [19–21]. In addition, a marginal band of modified stable MTs residing in the giant synaptic terminal of the goldfish retinal bipolar neuron mediates mitochondria transport and organization at synaptic terminals [18]. Finally, presynaptic MTs appear to regulate interswelling SV transport in mouse giant calyceal terminals [22], and interbouton dynamic MTs have been recently implicated in Kif1A-dependent delivery of SVs to distal boutons in hippocampal neurons [23]. It remains unknown, however, whether axonal *de novo* MT nucleation occurs post-development, is required for neurotransmission, and is a feature of neurons residing in an intact circuit.

Here, we describe that dynamic MTs emerge at excitatory presynaptic *en passant* boutons as a result of restricted  $\gamma$ -tubulin- and augmin-dependent *de novo* MT nucleation, with  $\gamma$ -tubulin regulating the nucleation density and augmin directing the uniform, plus-end-directed growth toward the distal end of the axon. Moreover, we found that *de novo* nucleation of dynamic MTs at boutons is conserved in an intact circuit, is stimulated by neuronal activity, and regulates neurotransmission by providing dynamic tracks for targeted interbouton transport of SVs.



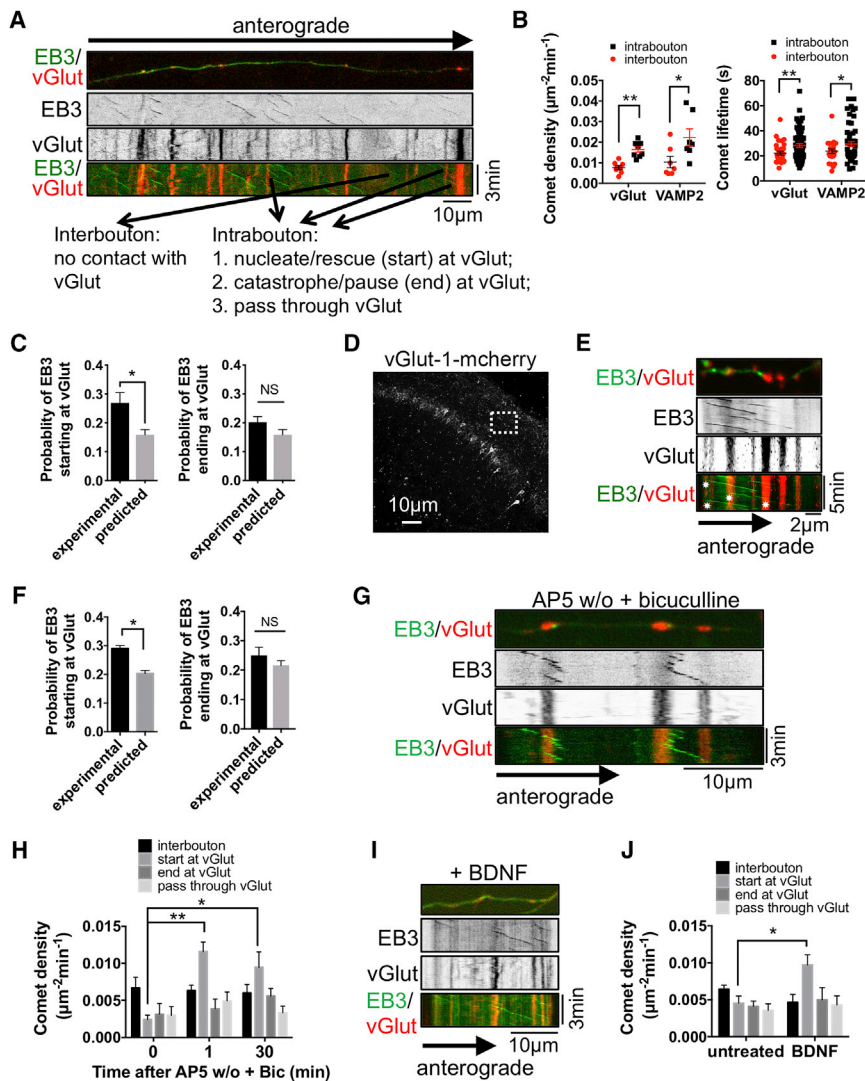


**Figure 1. Dynamic MT Plus Ends Initiate at Presynaptic Boutons upon Induction of Neuronal Activity**

(A) Representative maximum projection of spinning disk confocal fluorescence images and kymographs of untreated hippocampal neurons (21DIV) transfected with EB3-EGFP (EB3) and vGlut1-mCherry (vGlut) 24 h prior to live imaging (Figures S1A and S1B). Shown by arrows are the classifications of axonal dynamic MTs in inter- and intrabouton MTs as described.

(B) Comet density and lifetime of intrabouton and interbouton EB3 comets in neurons treated as in (A).

(C) Probability of EB3 comets starting or ending at vGlut<sup>+</sup> stable puncta from experimental observations or predicted random events. Experimental probability refers to the observed frequency of EB3 starting or ending at vGlut<sup>+</sup> stable puncta. Predicted probability refers to the chance of any EB3 comet to randomly start or end at vGlut, and it was calculated by taking the ratio of the observed number of vGlut<sup>+</sup> stable puncta  $\times$  the average diameter of a vGlut<sup>+</sup> stable punctum (1  $\mu\text{m}$ ) / axonal length ( $\mu\text{m}$ ).

(D) Representative maximum projection of spinning disk confocal fluorescence images of an acute hippocampal slice in the CA1 region from 21-day-old mice electroporated with EB3-EGFP and vGlut1-mCherry at E15.5. vGlut1-mCherry channel under a 20 $\times$  objective is shown, and the white dotted box indicates the axonal region selected for live imaging using a 60 $\times$  objective.

(E) Representative maximum projection of spinning disk confocal fluorescence image and kymographs of an axon from boxed region in (D) (Video S1). Asterisks indicate comet tracks initiating from vGlut<sup>+</sup> stable boutons.

(F) Probability of EB3 comets starting or ending at vGlut<sup>+</sup> stable puncta from experimental observations or predicted random events in axons from acute hippocampal slices.

(G and I) Representative kymographs of hippocampal neurons (21DIV) transfected with EB3 and vGlut and pretreated with 50  $\mu\text{M}$  of the NMDA receptor antagonist D-AP5 6–12 h prior to imaging, followed by a 1 min washout (w/o) and incubation with 20  $\mu\text{M}$  of the GABA<sub>A</sub> receptor antagonist bicuculline for up to 30 min (G) (Figures S1C–S1F; Video S2) or directly treated with 50 ng/mL BDNF for 1 min (I) (Figures S1G and S1H; Video S3).

(H and J) Subclassified comet density for intrabouton MTs measured in hippocampal neurons treated as in (G) or (I) for the indicated times. \* $p < 0.05$ ; \*\* $p < 0.01$ ; \*\*\* $p < 0.001$  by two-tailed Wilcoxon matched-pairs signed-rank tests (B, C, and F,  $N = 6$ –8 axons; H and J,  $N = 6$ –9 axons). NS, not significant.

## RESULTS

### Dynamic MT Plus Ends Emerge from Presynaptic Boutons in Axons of Hippocampal Neurons *In Vitro* and *Ex Vivo*

We examined the dynamic behavior of presynaptic MTs in axons of pyramidal neurons by transfecting cultured hippocampal neurons (18DIV) with EB3-EGFP and vGlut1-mCherry or VAMP2-mCherry constructs. Fast time-lapse imaging of EB3-labeled MT plus ends allows the quantitative assessment of MT dynamics at or away from individual glutamate release sites labeled with vGlut1-mCherry (Figures 1A and S1A). Presynaptic dynamic MTs were distinguished based on their plus-end contact with vGlut1<sup>+</sup> boutons and were defined as (1) *interbouton* MTs that have no contact with the presynaptic markers or (2) *intrabouton*

MTs that interact with the presynaptic synaptic vesicle marker at any point during their lifetime. Intrabouton MTs were further classified as (1) nucleating/rescuing (starting) at boutons, (2) undergoing catastrophe/pausing (ending) at the boutons, or (3) passing through the bouton (Figure 1A). Based on kymograph analyses of EB3 comet motion relative to the stable pool of two distinct presynaptic markers (vGlut1 and VAMP2; Figure S1A), we found a higher density of longer-lived intrabouton MTs than of interbouton MTs in untreated neurons (Figures 1B, S1A, and S1B). When we further analyzed the pool of intrabouton MTs that end or start at a bouton by measuring their observed frequencies compared to their relative probability predicted by chance, we found a significantly higher frequency of EB3 comets starting at rather than ending at presynaptic boutons (Figure 1C). This suggests that MT nucleation labeled by EB3 comets is

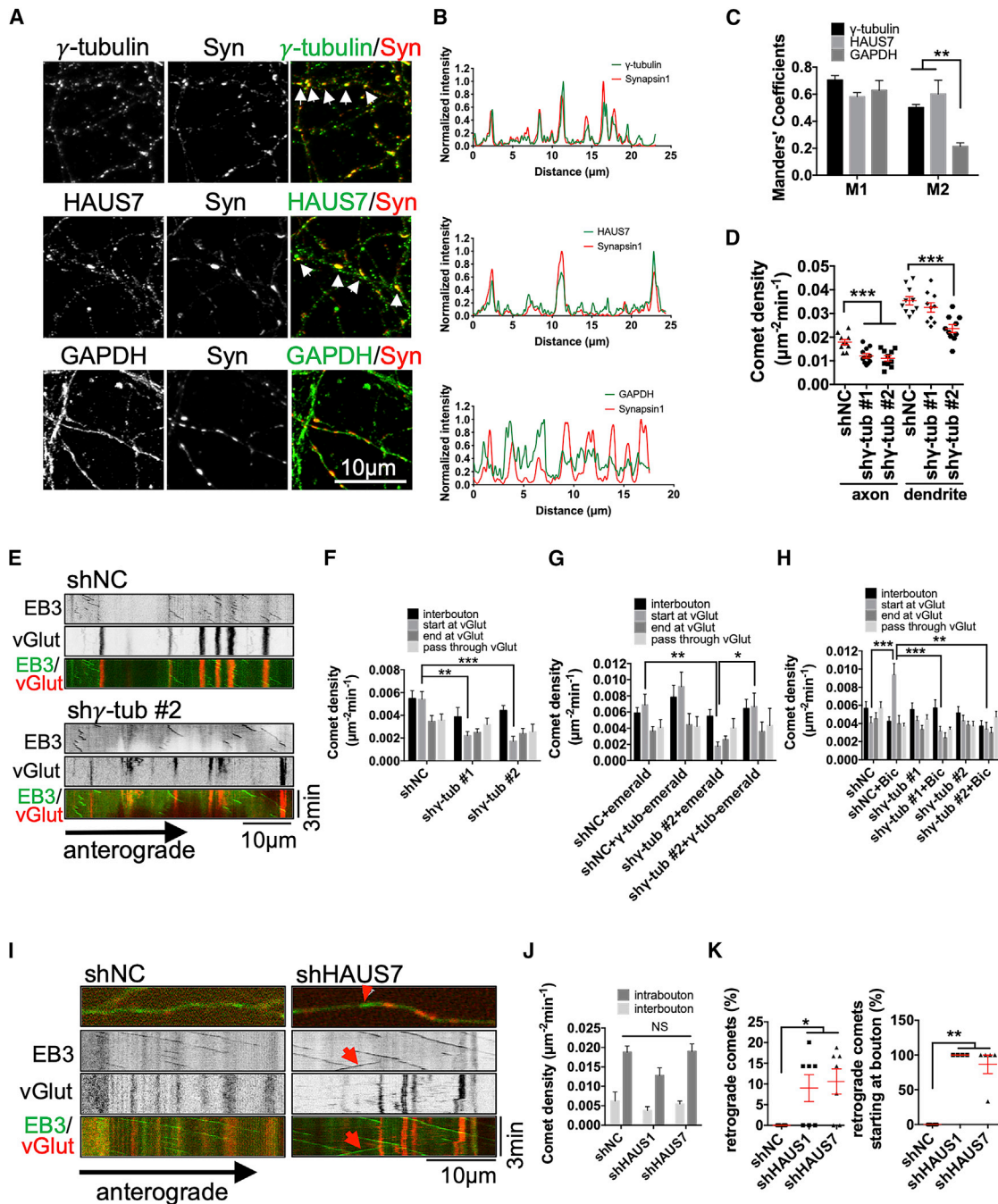


**Figure 2. Neuronal Activity Induces De Novo Nucleation of Distally Oriented Dynamic MTs through  $\gamma$ -Tubulin and Augmin Function at Presynaptic Boutons**

(A) Maximum projection of laser scanning confocal fluorescence images acquired with an Airyscan detector in hippocampal neurons (21DIV) fixed and stained for  $\gamma$ -tubulin, HAUS7, GAPDH, and synapsin-1 (Syn) (Figures S2A and S2B). White arrows indicate signals co-localizing with Syn.

(B) Normalized intensity of line scan of axons shown in (A) and indicated by arrows.

(C) Manders' coefficients of Syn<sup>+</sup> puncta co-localizing with  $\gamma$ -tubulin, HAUS7, or GAPDH. M1 refers to the fraction of Syn<sup>+</sup> puncta overlapping with  $\gamma$ -tubulin, HAUS7, or GAPDH; M2 refers to the fraction of  $\gamma$ -tubulin, HAUS7, or GAPDH overlapping with Syn<sup>+</sup> puncta.

(D and E) Quantification of EB3 comet density in axons and dendrites (D) and representative kymographs (E) of EB3 comets in axons of hippocampal neurons (20DIV) infected with noncoding control (shNC) or shRNA against  $\gamma$ -tubulin (sh $\gamma$ -tub #1 or sh $\gamma$ -tub #2) for 6 days (Figures S2C–S2F).

(F) Quantification of subclassified EB3 comet density relative to stable vGlut<sup>+</sup> puncta in axons of hippocampal neurons as in (E) (Figure S2G).

(G) Quantification of subclassified EB3 comet density relative to stable vGlut<sup>+</sup> puncta in axons of hippocampal neurons (20DIV) infected with shNC or sh $\gamma$ -tub #2 for 6 days and rescued by co-transfecting emerald control or human  $\gamma$ -tubulin-emerald that is resistant to lentiviral knockdown with EB3-tdTomato and vGlut1-mTAgBFP2 24 h prior to live imaging (Figures S2H–S2J).

(legend continued on next page)

frequently initiated at presynaptic boutons. To examine if this result is also observed *in situ* at synapses in a native circuit, we performed comparable time-lapse imaging of EB3-labeled dynamic MTs in close contact with stable vGlut1-labeled excitatory presynaptic boutons in the CA1 region of acute hippocampal slices isolated from 21-day-old mice that had been *in utero* co-electroporated with EB3-EGFP and vGlut1-mCherry at E15.5 (Figures 1D and 1E; Video S1). We observed a similar level of increase in frequency of EB3 comets starting, but not ending, at boutons compared to predicted random probability (Figure 1F), confirming the preferential regulation of EB3 comets initiating at presynaptic boutons *ex vivo* where cellular architecture and synaptic connectivity are largely intact.

We tested whether initiation of EB3 comets at boutons was regulated by action potential (AP)-driven neuronal activity, and we measured EB3 comet density starting at vGlut1<sup>+</sup> boutons upon either acute AP5/bicuculline treatment to increase AP firing (Figures 1G, 1H, S1C, and S1E; Video S2) or BDNF-induced neuronal activation (Figures 1I, 1J, S1G, and S1H; Video S3). Strikingly, both treatments resulted in a significant and specific increase in the density of comets initiating at vGlut1<sup>+</sup> boutons starting after 1 min of treatment, but not in D-AP5 washout or untreated control conditions (Figure S1D). In addition, the percentage of nucleated comets reaching the next distal bouton increased by 3-fold upon acute neuronal firing, as we observed that the MTs that started at a bouton preferentially reached to the next bouton rather than stopping before or passing through the next bouton (Figure S1F). Together, these data demonstrate that initiation of dynamic MT plus ends preferentially occurs at presynaptic sites, shows biased directionality being almost always oriented toward the distal tip of the axon, and can be induced by neuronal activity.

### Activity-Promoted Initiation of Distally Oriented Dynamic MT Plus Ends at Boutons Results from $\gamma$ -Tubulin- and Augmin-Dependent *De Novo* MT Nucleation

The increase in distally oriented EB3 comets could either result from *de novo* nucleation by  $\gamma$ -tubulin or from polymerization from preexisting MTs by the activity of MT rescue factors. In axons of developing neurons,  $\gamma$ -tubulin is required for centrosomal MT organization, and the augmin complex interacts with  $\gamma$ TuRC to control MT distal polarity [24, 25]. However, whether axonal MT nucleation in the shaft and/or at presynaptic contacts occurs in axons of neurons with mature synapses is currently unknown. First, we examined endogenous  $\gamma$ -tubulin localization relative to the presynaptic marker synapsin-1 in 21DIV hippocampal neurons, and we found that  $\gamma$ -tubulin signal co-localized with synapsin-1<sup>+</sup> puncta  $\sim$ 2.5 fold more than GAPDH cytosolic

control (Figures 2A–2C). Similarly,  $\sim$ 80% of exogenously expressed  $\gamma$ -tubulin-emerald co-localized with stable vGlut1-mCherry<sup>+</sup> (vGlut) puncta in 21DIV hippocampal neurons compared to  $\sim$ 50% of emerald control (Figures S2A and S2B).

When we knocked down endogenous  $\gamma$ -tubulin in hippocampal neurons for 6 days with 2 different shRNAs, we achieved either  $\sim$ 50% (sh $\gamma$ -tub #1) or  $\sim$ 60% (sh $\gamma$ -tub #2) protein depletion and observed a significant decrease in comet density, growth rates, catastrophe/pausing, and rescue frequencies of EB3-EGFP or endogenous EB3 puncta and dynamic MTs in both axons and dendrites (Figures 2D and S2C–S2J). Interestingly, the decrease in comet density in axons was most significantly from loss of EB3 comets starting at presynaptic boutons (Figures 2E and 2F) and was completely rescued by re-expressing shRNA-resistant human  $\gamma$ -tubulin-emerald but not its emerald control (Figure 2G). Silencing of  $\gamma$ -tubulin for 4 days, however, a condition that did not interfere with comet density or MT stability in unstimulated neurons (Figures 2H, S2I, and S2J), significantly abrogated only the increase in the density of EB3 comets starting at boutons upon induction of neuronal activity (Figure 2H). These data strongly indicate that dynamic MTs initiating at excitatory boutons are a result of  $\gamma$ -tubulin-dependent *de novo* nucleation and that presynaptic boutons are hotspots for activity-evoked MT nucleation in axons.

Nearly all newly nucleated MTs at presynaptic boutons displayed a biased growth orientation, with 96.4% of total intrabouton comets (N = 55) and 100% of the comets initiating at boutons (N = 24) moving toward the distal tip of the axon. The augmin complex regulates the polarity of  $\gamma$ -tubulin-nucleated MTs in non-neuronal cells and in axons of developing neurons, with  $\gamma$ -tubulin providing the nucleating material and the augmin complex being important for the maintenance of uniform polarity of axonal MTs [24, 25]. We found that the endogenous augmin complex subunit HAUS7 co-localized with synapsin-1<sup>+</sup> boutons more significantly than cytosolic GAPDH (Figures 2A–2C). In addition, silencing of the augmin complex expression by knocking down subunits HAUS1 or HAUS7 to an extent ( $\sim$ 40% of protein depletion) (Figures S2K and S2L) that had no effect on comet density per se significantly increased the percentage of retrograde comets, almost all of which initiated at boutons (Figures 2I–2K; Video S4).

Collectively, these data indicate that  $\gamma$ -tubulin and augmin are preferentially localized at excitatory *en passant* boutons, where they are required for activity-dependent *de novo* nucleation of uniformly distally oriented dynamic MTs.

### MT Nucleation at Boutons Is Required for SV Interbouton Bidirectional Motility and Neurotransmission

We investigated whether *de novo* nucleated dynamic MTs at boutons could provide the tracks for activity-evoked motility of

(H) Quantification of subclassified EB3 comet density relative to stable vGlut<sup>+</sup> puncta of hippocampal neurons (18DIV) infected with shNC or sh $\gamma$ -tub#1 or #2 for 4 days and transfected with EB3-EGFP (EB3) and vGlut1-mCherry 24 h prior to live imaging. Neurons were pretreated with D-AP5 6–12 h prior to imaging, followed by a washout and incubation with bicuculline for 1–10 min (+Bic).

(I) Kymographs of hippocampal neurons (21DIV) infected with shNC or shRNAs against HAUS1 or HAUS7 for 7 days (Figures S2K and S2L) and transfected with EB3-EGFP (EB3) and vGlut1-mCherry (vGlut) 24 h prior to live imaging (Video S4). Red arrows show a retrogradely oriented EB3 comet initiating from a bouton.

(J) Quantification of intra- and interbouton comet density in neurons treated as in (I).

(K) Quantification of the percentage of retrograde comets and retrograde comets starting at boutons of neurons as in (H). \*p < 0.05; \*\*p < 0.01; \*\*\*p < 0.001 by Mann-Whitney test (C, N = 10 axons), Kruskal-Wallis tests with Dunn's multiple comparisons tests (D and F, N = 10 = 12 axons; G, N = 5 axons; J and K, N = 6–7 axons), and two-tailed Wilcoxon matched-pairs signed rank test (H, N = 10–12 axons). NS, not significant.

axonal cargos [26–29]. To this end, we analyzed the dynamics of a wide range of axonal organelles as well as SVs relative to vGlut1<sup>+</sup> stable presynaptic boutons in a time window during which we observed MT nucleation at boutons upon induction of neuronal activity. No substantial change was detected in Rab5 (early endosome marker; Figure S3A), Rab7 (late endosome marker; Figure S3B), LAMP1 (lysosome marker; Figure S3C), or mitochondria dynamics (Figure S3D), indicating that motility of these organelles is not immediately affected by activation of neuronal activity induced by bicuculline. We observed, however, a significant increase in the percentage of motile vGlut1<sup>+</sup>, synaptophysin<sup>+</sup>, and Arl8b<sup>+</sup> SVs that would start or end at stable presynaptic boutons (Figures 3A–3D, S3I, and S3J), with no preference in the direction of the movement (Figures S3E, S3F, and S3K). We measured and plotted the % of vGlut1<sup>+</sup> SVs that ended, started, or started and ended at a bouton upon evoked MT nucleation and found a 15% increase in the pool of SVs that would end at a bouton and an almost 3-fold increase in the % of SVs that would start at a bouton and reach to the next one (Figure 3D). Interestingly, we observed a very similar fold increase in the density of comets initiated at one bouton and reaching to the next distal one (Figure S1F), suggesting the bidirectional interbouton transport of SVs upon neuronal stimulation is regulated by *de novo* nucleated MTs that provide tracks for the targeted delivery of pools of SVs between neighboring boutons.

To further understand whether local SV transport is dependent on *de novo* MT nucleation, we examined the mobile pool of vGlut1<sup>+</sup>, synaptophysin<sup>+</sup>, and Arl8b<sup>+</sup> SVs in neurons depleted of  $\gamma$ -tubulin expression for 4 days to levels that would only affect activity-evoked MT nucleation at boutons. Remarkably, we found that  $\gamma$ -tubulin knockdown strongly inhibited activity-evoked motility of SVs toward and away from the boutons (Figures 3E–3J) with no preference in either anterograde or retrograde direction (Figures S3G, S3H, and S3L). This demonstrates that activity-evoked MT nucleation at boutons is required for stimulated SV targeted interbouton delivery.

Inhibition of Arl8-mediated transport of SVs and presynaptic lysosome-related vesicles (PLVs) affects bouton size and neurotransmission during bouton biogenesis [30, 31]. Thus, we examined whether dynamic MTs nucleated at boutons could affect SV pool size and/or exocytosis kinetics at presynaptic release sites of neurons with mature synapses. To this end, the pH-sensitive vesicular chimeric marker vGlut1-pHluorin and the cytosolic filler mCherry-C1 were co-transfected into neurons (16DIV) that had been depleted of  $\gamma$ -tubulin expression by two independent shRNAs to levels that would only affect evoked-MT nucleation at boutons (4 days of silencing). We measured no significant difference in vGlut1-pHluorin signal intensity at active presynapses after alkalinization with NH<sub>4</sub>Cl. However, a marked reduction of high-frequency (10 Hz) stimulated fluorescence in  $\gamma$ -tubulin-depleted neurons was observed compared to control neurons, indicating that loss of AP-evoked MT nucleation at boutons strongly inhibited activity-stimulated exocytosis without altering the total pool of SVs residing at boutons (Figures 4A–4E). A more dramatic inhibition of stimulated fluorescence and a trend toward a decrease in the size of the total SV pool were observed in neurons depleted of  $\gamma$ -tubulin expression for 6 days (Figures S4D–S4H). This also resulted in a significant reduction in the % of total moving SVs in naive neurons in contrast to loss of augmin

expression, which did not detectably affect SV motility in either direction (Figures S4A–S4C).

Ca<sup>2+</sup> influx through voltage-gated Ca<sup>2+</sup> channels plays a crucial role in exocytosis, and the strong inhibition of AP-triggered exocytosis upon  $\gamma$ -tubulin depletion could potentially be due to decreased Ca<sup>2+</sup> entry. We examined the impact of loss of  $\gamma$ -tubulin expression on AP-evoked Ca<sup>2+</sup> entry [32], and although in our assays we could not differentiate between calcium influx from the external environment or calcium efflux from internal stores, we found that depleting  $\gamma$ -tubulin expression for 4 days (Figures 4F and 4G) or 6 days (Figures S4I and S4J) did not reduce AP-evoked Ca<sup>2+</sup> accumulation at boutons, ruling out suppression of an increase in intracellular Ca<sup>2+</sup> at boutons as a mechanism of the observed inhibition of presynaptic release.

Together, these data indicate that activity-stimulated *de novo* MT nucleation at boutons controls SV interbouton transport and neurotransmitter release.

## DISCUSSION

We found that in primary hippocampal neurons, excitatory *en passant* boutons are hotspots for  $\gamma$ -tubulin-dependent MT nucleation that is induced by neuronal activity. Importantly, MT nucleation preferentially occurs at excitatory boutons in hippocampal slices from neonatal mice, demonstrating that localized MT nucleation at boutons is a bona fide feature of mature hippocampal neurons residing in tissue where cytoarchitecture and synaptic organization are preserved (Figure 1).

$\gamma$ -tubulin had been shown to control acentrosomal MT nucleation, neuronal polarity, and axonal outgrowth in developing dendrites and axons [25, 33]. The present study reports a nucleating function of  $\gamma$ -tubulin in mature synapses that is compartmentalized, regulated by neuronal activity, and rate limiting for synaptic transmission.

In axons, we found that acute  $\gamma$ -tubulin knockdown preferentially affected MT initiation from the boutons, suggesting that MT initiation at boutons results from localized  $\gamma$ -tubulin nucleating activity (Figures 2 and S2). Although we cannot formally rule out an unknown  $\gamma$ -tubulin MT rescue function at boutons or an effect of incomplete  $\gamma$ -tubulin depletion at interboutons, our data indicate that it is the MT nucleating activity of  $\gamma$ -tubulin to be required for MT initiation at boutons in response to neuronal activity and that interbouton comet density may be regulated by either MT rescue factors or a yet-unknown non- $\gamma$ -tubulin-dependent MT nucleating machinery such as the recently discovered MT remodeling factor SSNA1 [34]. In support of our interpretation, we further demonstrate that the correct polarity of presynaptic *de novo* nucleated MTs requires the augmin complex and that similarly to  $\gamma$ -tubulin, augmin<sup>+</sup> puncta are preferentially localized at *en passant* presynaptic boutons compared to a cytosolic protein (Figure 2). Augmin complex depletion, however, had no impact on MT polarity in dendrites, as antiparallel MT organization could be regulated by other mechanisms [2, 24]. It was previously shown that in axons of developing neurons,  $\gamma$ -tubulin is required for acentrosomal MT organization, and the augmin complex interacts with  $\gamma$ TuRC to control conserved polarity [24, 25]. Our results not only demonstrate that the augmin complex restricts the uniform

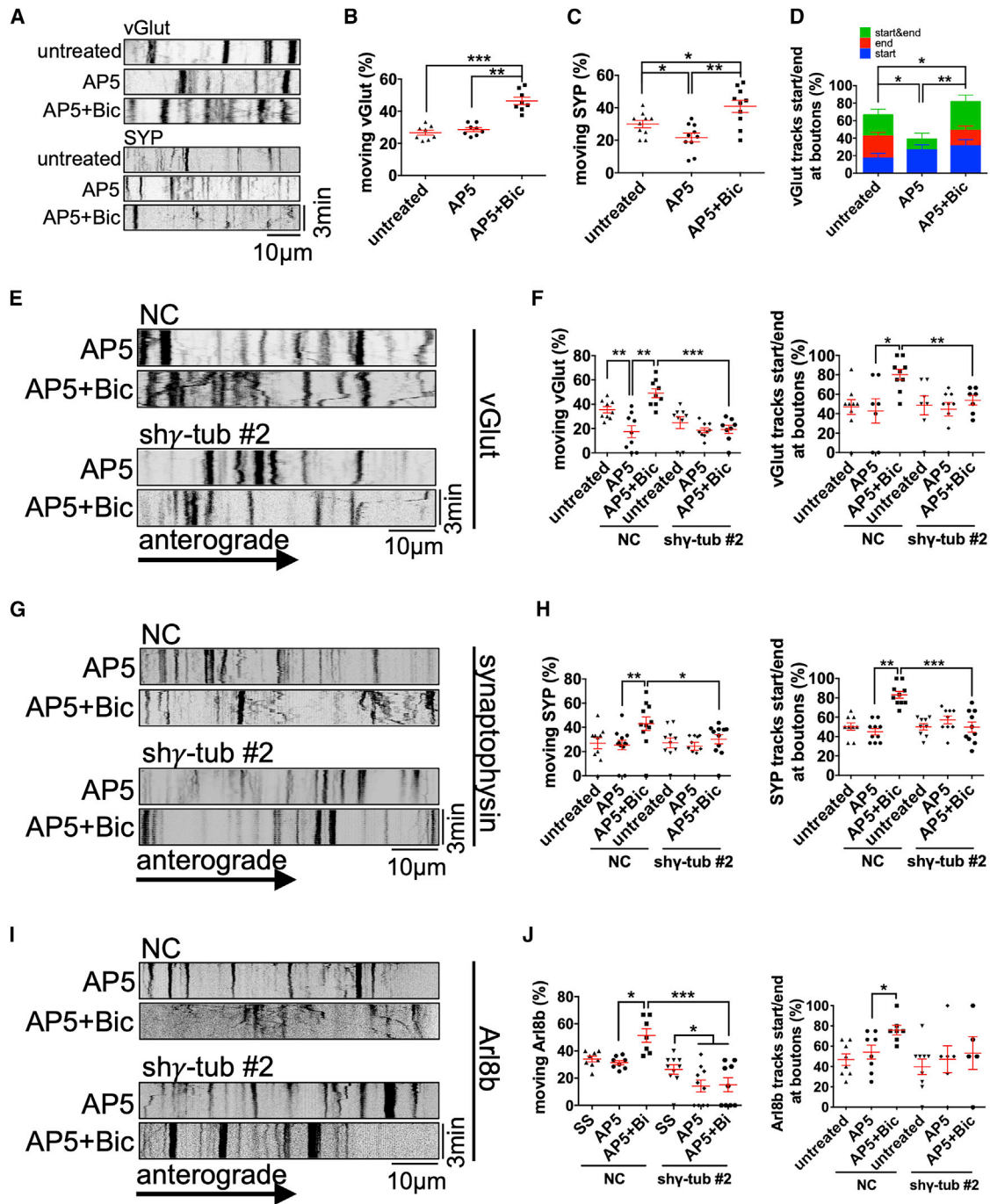


**Figure 3. MT Nucleation at Boutons Is Required for Bidirectional SV Interbouton Movement Stimulated by Neuronal Activity**

(A–D) Representative kymographs (A) and quantification of the percentage of moving vGlut<sup>+</sup> (B) or synaptophysin<sup>+</sup> (SYP) (C) puncta and percentage of moving vGlut<sup>+</sup> puncta starting and/or ending at boutons out of moving vGlut<sup>+</sup> population (D) in untreated hippocampal neurons (18DIV) or AP5-pretreated neurons before and after a washout with bicuculline. Neurons were transfected with EB3-EGFP and vGlut1-mCherry (B) or EB3-tdTomato and SYP-Venus (C), and vGlut1-mTAGBFP2 24 h prior to live imaging (Figures S3A–S3F, and S1I–S1K).

(E, G, and I) Representative kymographs of vGlut<sup>+</sup> (E), SYP<sup>+</sup> (G), or Arl8b<sup>+</sup> (I) puncta in hippocampal neurons (18DIV) infected with noncoding control (shNC) or shRNA against  $\gamma$ -tubulin (shy-tub #2) for 4 days and treated as in (A) and (B) or transfected with EB3-tdTomato and Arl8b-EGFP (I) (Figures S3G, S3H, and S3L). (F, H, and J) Quantification of the percentage of moving vGlut<sup>+</sup> (F), SYP<sup>+</sup> (H), or Arl8b<sup>+</sup> (J) puncta and the percentage of moving tracks starting or ending at boutons out of moving vGlut<sup>+</sup> (F), SYP<sup>+</sup> (H), and Arl8b<sup>+</sup> (J) puncta populations in hippocampal neurons treated as in (E), (G), or (I). \*p < 0.05; \*\*p < 0.01; \*\*\*p < 0.001 by Mann-Whitney tests comparing untreated and AP5 washout with bicuculline and Wilcoxon matched-pairs signed-rank tests comparing before and after AP5 washout with bicuculline (N = 8–12 axons).

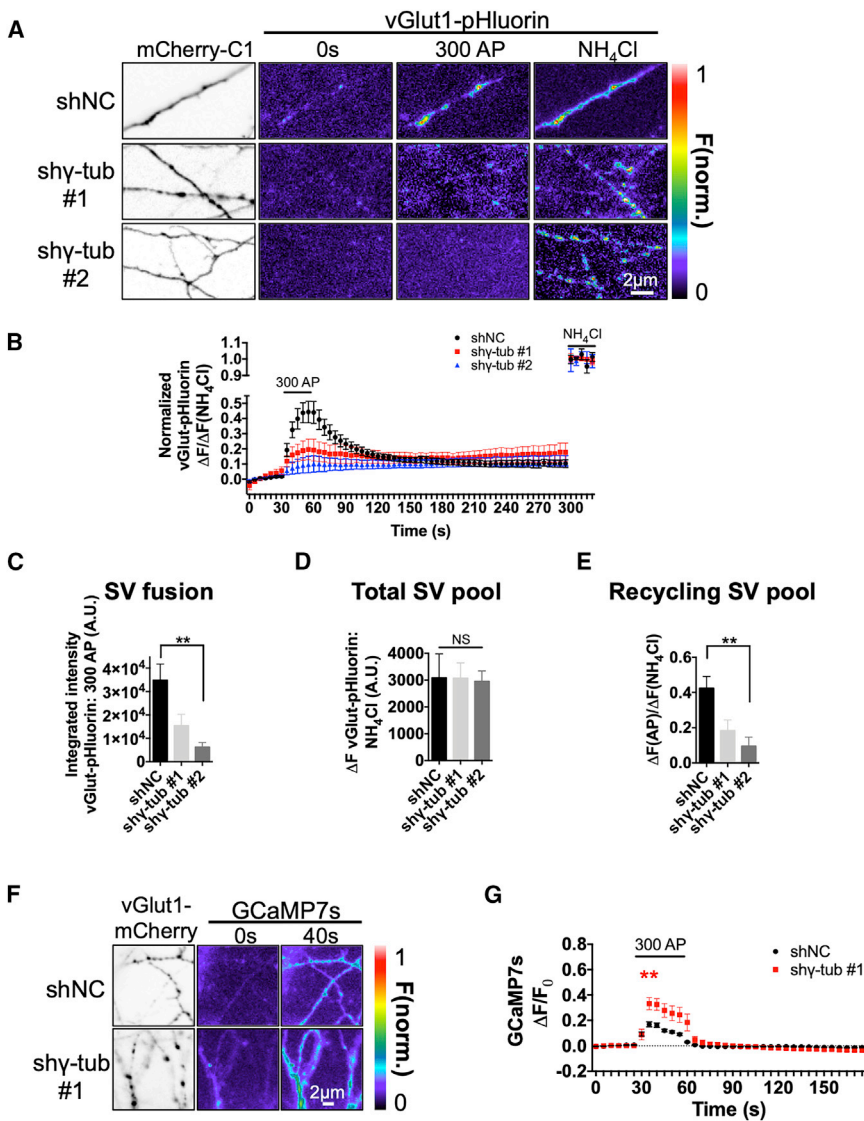


**Figure 4. MT Nucleation at Boutons Controls SV Exocytosis**

(A) Representative images of hippocampal neurons (16DIV) infected with noncoding control (shNC) or two independent shRNAs against  $\gamma$ -tubulin (sh $\gamma$ -tub #1 or #2) for 4 days and co-transfected with vGlut1-pHluorin and mCherry-C1 prior to recording vGlut1-pHluorin dequenching for the indicated times in response to neuronal activation induced by 300 action potentials (APs) at 10 Hz starting from 30 s (Figure S4).

(B) Normalized fluorescence change ( $\Delta F$ ) over total vGlut1-pHluorin ( $\Delta F$  upon NH<sub>4</sub>Cl dequenching) at the indicated times.

(C) Integrated intensity of vGlut1-pHluorin signal during the 300 AP stimulation paradigm.

(D) Total pool of SVs indicated by vGlut1-pHluorin signal intensity at active presynapses after alkalization with NH<sub>4</sub>Cl.

(E) Recycling pool of SVs indicated by the ratio of  $\Delta F$  at maximum stimulation over  $\Delta F$  after alkalization with NH<sub>4</sub>Cl.

(F) Representative images of hippocampal neurons (16DIV) infected with shNC or shy-tub #2 lentiviruses for 4 days and co-transfected with GCaMP7s and vGlut1-mCherry using the same stimulation protocol as in (A).

(G) Ratio of GCaMP fluorescence change ( $\Delta F$ ) over baseline intensity ( $F_0$ ) at the indicated times. \* $p < 0.05$ ; \*\* $p < 0.01$ ; \*\*\* $p < 0.001$  by Mann-Whitney tests (A–E,  $N = 4$ –6 imaging fields including 8–18 axons with 200–360 boutons; F and G,  $N = 3$ –4 imaging fields including 6–12 axons with 120–150 boutons). Red asterisk in (G) compares  $\gamma$ -tubulin #2 to control levels at 40 s.

orientation of dynamic MTs at presynaptic boutons of mature axons but further support the notion that these newly generated presynaptic MTs result from *de novo*  $\gamma$ -tubulin nucleation rather than MT rescue or SSNA1-mediated protofilament splitting. How mature axons and selected boutons preferentially activate the augmin complex in coordination with  $\gamma$ -tubulin for the initiation of oriented MT nucleation upon neuronal firing remains to be established.

We found that at basal levels, both endogenous and overexpressed  $\gamma$ -tubulin<sup>+</sup> puncta and the HAUS7 subunit of the augmin complex are localized at *en passant* presynaptic boutons 2.5- ( $\gamma$ -tubulin) or 3- (HAUS7) fold more frequently compared to the cytosolic marker GAPDH (Figure 2). The basis for this selective localization is at the moment unknown but may reflect modulation of SV releasing activity at individual synapses and/or the ability of a bouton to establish functional contacts with a postsynaptic site. Future investigation is needed to detail the mechanisms of  $\gamma$ -tubulin and augmin recruitment to presynaptic boutons and the rules establishing bouton selection.

proteins in developing neurons during presynaptic biogenesis [30, 31, 35]. In addition, Kif1A was recently implicated in synaptic cargo anterograde delivery to *en passant* boutons using dynamic MTs as tracks [23]. Based on this collective evidence, we propose a model in which dynamic MTs are *de novo* nucleated to serve as tracks for targeted bidirectional interbouton delivery of a rate-limiting supply of SVs at sites of stimulated release. Whether these SVs represent a unique pool destined to interbouton delivery to provide for efficient exocytosis or two different pools with distinct rate-limiting components depending on the direction of delivery (distal versus proximal) remains to be established. Indeed, our observation that neuronal activity stimulates presynaptic *de novo* nucleation of dynamic MTs that terminate at the next distal bouton is in line with the findings that *en passant* boutons are enriched in dynamic MT plus ends [23]. Our results differ in that we observed that (1) only MT nucleation (initiation), but not catastrophe/pausing (termination), is preferentially regulated at boutons at basal levels, and (2) both anterograde and retrograde SV transport are equally dependent on MT nucleation

at boutons (Figures 3 and S3). The discrepancy may perhaps be explained because, in contrast to their measurements which spanned along the entire length of the axon, our *in vitro* and *ex vivo* comet tracking were restricted to proximal axons, a region where interbouton bidirectional transport of pools of SVs predominates [23, 36–39]. The model that Guedes-Dias et al. [23] propose may be more consistent with targeted long-distance delivery and retention of SV precursors to synapses residing in the most distal region of the axon. At proximal synaptic sites, however, a higher proportion of bidirectional interbouton delivery of SVs may be required in response to neuronal activation. This is consistent with our observation that in proximal axons, ~40% of nucleated comets at a bouton reach to the next bouton after bicuculline-induced firing, compared to ~10% before stimulation in dissociated hippocampal neurons (Figure S1) or ~25% in hippocampal slices.

We found that loss of *de novo* nucleated MTs by  $\gamma$ -tubulin depletion significantly impairs high-frequency evoked-neurotransmitter release, paving the way for the characterization of the mechanisms by which presynaptic dynamic MTs may accomplish this task through targeted delivery of a rate-limiting pool of SVs to the sites of fusion and/or by mediating the transport of a rate-limiting vesicular component of the fusion or AZ machinery.

At present, the signaling pathways that regulate presynaptic MT nucleation are unknown. One hypothesis is that neuronal firing may drive  $\text{Ca}^{2+}$  influx-dependent activation of MT nucleation complexes at boutons. Given the critical role that loss of a functional presynaptic machinery for MT nucleation may have for neurotransmission, it will be important to determine the *in vivo* significance of this selective MT nucleation and whether dysregulation of this process can be associated with human neurological and neuropsychiatric illnesses caused by mutations in MT regulatory proteins residing presynaptically, such as tau in AD [40, 41] and tauopathies, spastin in hereditary spastic paraplegias [42, 43], and MAP1B and FMRP in fragile X syndrome [44–46].

## STAR★METHODS

Detailed methods are provided in the online version of this paper and include the following:

- KEY RESOURCES TABLE
- LEAD CONTACT AND MATERIALS AVAILABILITY
- EXPERIMENTAL MODEL AND SUBJECT DETAILS
  - Primary hippocampal neuronal cultures
  - Acute hippocampal slices
- METHOD DETAILS
  - Lentiviral shRNA silencing
  - Western blot analyses
  - Immunofluorescence microscopy and analyses
  - Live imaging of MT, organelle and SV dynamics
  - *In utero* electroporation and live-imaging of acute hippocampal slices
  - Live imaging of SV exo-/endocytosis
  - Live imaging of  $\text{Ca}^{2+}$  influx by GCaMP7s
- QUANTIFICATION AND STATISTICAL ANALYSIS
- DATA AND CODE AVAILABILITY

## SUPPLEMENTAL INFORMATION

Supplemental Information can be found online at <https://doi.org/10.1016/j.cub.2019.10.049>.

## ACKNOWLEDGMENTS

Our gratitude goes to Franck Polleux for providing us with the *ex vivo* experimental set up, EB3-EGFP, mito-DsRed2, synaptophysin-Venus, and vGlut1-mTagBFP2 constructs, in addition to helpful discussions; Viktoriya Zhuravleva for assisting us with the vGlut1-pHluorin experimental set up; Inbal Israely for sharing pCMV-GCaMP7s construct; Richard Vallee for sharing EGFP-Rab7a construct; Volker Haucke for sharing LAMP1-EGFP and ARI8b-EGFP constructs; and Ryan Bose-Roy for helping with the analysis of the movies. We are grateful to Gregg G. Gunderson and Richard Vallee for access to their microscopes. This project was funded by an RO1AG050658 (NIH/NIA) to F.B.

## AUTHOR CONTRIBUTIONS

X.Q. and F.B. designed the project, analyzed all the data, and wrote the manuscript. X.Q. performed most of the experiments. H.B. carried out the *in utero* hippocampal electroporation. A.K. and H.B. performed the *ex vivo* time-lapse imaging experiment with acute hippocampal slices. vGlut1-Phluorin and GCaMP7s experiments in hippocampal neurons were carried out by A.K. under C.W.'s supervision.

## DECLARATION OF INTERESTS

The authors declare no conflicts of interest.

Received: June 20, 2019

Revised: September 24, 2019

Accepted: October 24, 2019

Published: December 5, 2019

## REFERENCES

1. Dent, E.W. (2017). Of microtubules and memory: implications for microtubule dynamics in dendrites and spines. *Mol. Biol. Cell* 28, 1–8.
2. Kapitein, L.C., and Hoogenraad, C.C. (2015). Building the neuronal microtubule cytoskeleton. *Neuron* 87, 492–506.
3. Nirschl, J.J., Ghirelli, A.E., and Holzbaur, E.L.F. (2017). The impact of cytoskeletal organization on the local regulation of neuronal transport. *Nat. Rev. Neurosci.* 18, 585–597.
4. Gu, J., Firestein, B.L., and Zheng, J.Q. (2008). Microtubules in dendritic spine development. *J. Neurosci.* 28, 12120–12124.
5. Hu, X., Viesselmann, C., Nam, S., Merriam, E., and Dent, E.W. (2008). Activity-dependent dynamic microtubule invasion of dendritic spines. *J. Neurosci.* 28, 13094–13105.
6. Jaworski, J., Kapitein, L.C., Gouveia, S.M., Dortland, B.R., Wulf, P.S., Grigoriev, I., Camera, P., Spangler, S.A., Di Stefano, P., Demmers, J., et al. (2009). Dynamic microtubules regulate dendritic spine morphology and synaptic plasticity. *Neuron* 61, 85–100.
7. Kapitein, L.C., Yau, K.W., Gouveia, S.M., van der Zwan, W.A., Wulf, P.S., Keijzer, N., Demmers, J., Jaworski, J., Akhmanova, A., and Hoogenraad, C.C. (2011). NMDA receptor activation suppresses microtubule growth and spine entry. *J. Neurosci.* 31, 8194–8209.
8. McVicker, D.P., Awe, A.M., Richters, K.E., Wilson, R.L., Cowdrey, D.A., Hu, X., Chapman, E.R., and Dent, E.W. (2016). Transport of a kinesin-cargo pair along microtubules into dendritic spines undergoing synaptic plasticity. *Nat. Commun.* 7, 12741.
9. Merriam, E.B., Millette, M., Lombard, D.C., Saengsawang, W., Fothergill, T., Hu, X., Ferhat, L., and Dent, E.W. (2013). Synaptic regulation of microtubule dynamics in dendritic spines by calcium, F-actin, and drebrin. *J. Neurosci.* 33, 16471–16482.

10. Gray, E.G. (1959). Axo-somatic and axo-dendritic synapses of the cerebral cortex: an electron microscope study. *J. Anat.* **93**, 420–433.
11. Gray, E.G. (1975). Presynaptic microtubules and their association with synaptic vesicles. *Proc. R. Soc. Lond. B Biol. Sci.* **190**, 367–372.
12. Gray, E.G. (1976). Problems of understanding the substructure of synapses. *Prog. Brain Res.* **45**, 207–234.
13. Gray, E.G. (1978). Synaptic vesicles and microtubules in frog motor endplates. *Proc. R. Soc. Lond. B Biol. Sci.* **203**, 219–227.
14. Gray, E.G., Burgoyne, R.D., Westrum, L.E., Cumming, R., and Barron, J. (1982). The enigma of microtubule coils in brain synaptosomes. *Proc. R. Soc. Lond. B Biol. Sci.* **216**, 385–396.
15. Gray, E.G., Westrum, L.E., Burgoyne, R.D., and Barron, J. (1982). Synaptic organisation and neuron microtubule distribution. *Cell Tissue Res.* **226**, 579–588.
16. Westrum, L.E., and Gray, E.G. (1977). Microtubules associated with post-synaptic ‘thickenings’. *J. Neurocytol.* **6**, 505–518.
17. Westrum, L.E., Gray, E.G., Burgoyne, R.D., and Barron, J. (1983). Synaptic development and microtubule organization. *Cell Tissue Res.* **231**, 93–102.
18. Graffe, M., Zenisek, D., and Taraska, J.W. (2015). A marginal band of microtubules transports and organizes mitochondria in retinal bipolar synaptic terminals. *J. Gen. Physiol.* **146**, 109–117.
19. Pawson, C., Eaton, B.A., and Davis, G.W. (2008). Formin-dependent synaptic growth: evidence that Dlar signals via Diaphanous to modulate synaptic actin and dynamic pioneer microtubules. *J. Neurosci.* **28**, 11111–11123.
20. Roos, J., Hummel, T., Ng, N., Klämbt, C., and Davis, G.W. (2000). *Drosophila* Futsch regulates synaptic microtubule organization and is necessary for synaptic growth. *Neuron* **26**, 371–382.
21. Migh, E., Götz, T., Földi, I., Szikora, S., Gombos, R., Darula, Z., Medzihradzky, K.F., Maléth, J., Hegyi, P., Sigrist, S., and Mihály, J. (2018). Microtubule organization in presynaptic boutons relies on the formin DAAM. *Development* **145**, dev158519.
22. Guillaud, L., Dimitrov, D., and Takahashi, T. (2017). Presynaptic morphology and vesicular composition determine vesicle dynamics in mouse central synapses. *eLife* **6**, e24845.
23. Guedes-Dias, P., Nirschl, J.J., Abreu, N., Tokito, M.K., Janke, C., Magiera, M.M., and Holzbaur, E.L.F. (2019). Kinesin-3 responds to local microtubule dynamics to target synaptic cargo delivery to the presynapse. *Curr. Biol.* **29**, 268–282.e268.
24. Cunha-Ferreira, I., Chazeau, A., Buijs, R.R., Stucchi, R., Will, L., Pan, X., Adolfs, Y., van der Meer, C., Wolthuis, J.C., Kahn, O.I., et al. (2018). The HAUS complex is a key regulator of non-centrosomal microtubule organization during neuronal development. *Cell Rep.* **24**, 791–800.
25. Sánchez-Huertas, C., Freixo, F., Viais, R., Lacasa, C., Soriano, E., and Lüders, J. (2016). Non-centrosomal nucleation mediated by augmin organizes microtubules in post-mitotic neurons and controls axonal microtubule polarity. *Nat. Commun.* **7**, 12187.
26. Moughamian, A.J., Osborn, G.E., Lazarus, J.E., Maday, S., and Holzbaur, E.L. (2013). Ordered recruitment of dynein to the microtubule plus-end is required for efficient initiation of retrograde axonal transport. *J. Neurosci.* **33**, 13190–13203.
27. Nirschl, J.J., Magiera, M.M., Lazarus, J.E., Janke, C., and Holzbaur, E.L. (2016).  $\alpha$ -tubulin tyrosination and CLIP-170 phosphorylation regulate the initiation of dynein-driven transport in neurons. *Cell Rep.* **14**, 2637–2652.
28. Okada, Y., Yamazaki, H., Sekine-Aizawa, Y., and Hirokawa, N. (1995). The neuron-specific kinesin superfamily protein KIF1A is a unique monomeric motor for anterograde axonal transport of synaptic vesicle precursors. *Cell* **81**, 769–780.
29. Yamazaki, H., Nakata, T., Okada, Y., and Hirokawa, N. (1995). KIF3A/B: a heterodimeric kinesin superfamily protein that works as a microtubule plus end-directed motor for membrane organelle transport. *J. Cell Biol.* **130**, 1387–1399.
30. Klassen, M.P., Wu, Y.E., Maeder, C.I., Nakae, I., Cueva, J.G., Lehrman, E.K., Tada, M., Gengyo-Ando, K., Wang, G.J., Goodman, M., et al. (2010). An Arf-like small G protein, ARL-8, promotes the axonal transport of presynaptic cargoes by suppressing vesicle aggregation. *Neuron* **66**, 710–723.
31. Vukoja, A., Rey, U., Petzoldt, A.G., Ott, C., Vollweiler, D., Quentin, C., Puchkov, D., Reynolds, E., Lehmann, M., Hohensee, S., et al. (2018). Presynaptic biogenesis requires axonal transport of lysosome-related vesicles. *Neuron* **99**, 1216–1232.e1217.
32. Dana, H., Sun, Y., Mohar, B., Hulse, B.K., Kerlin, A.M., Hasseman, J.P., Tsegaye, G., Tsang, A., Wong, A., Patel, R., et al. (2019). High-performance calcium sensors for imaging activity in neuronal populations and microcompartments. *Nat. Methods* **16**, 649–657.
33. Nguyen, M.M., McCracken, C.J., Milner, E.S., Goetschius, D.J., Weiner, A.T., Long, M.K., Michael, N.L., Munro, S., and Rolls, M.M. (2014).  $\Gamma$ -tubulin controls neuronal microtubule polarity independently of Golgi outposts. *Mol. Biol. Cell* **25**, 2039–2050.
34. Basnet, N., Nedožralova, H., Crevenna, A.H., Bodakuntla, S., Schlichthaerle, T., Taschner, M., Cardone, G., Janke, C., Jungmann, R., Magiera, M.M., et al. (2018). Direct induction of microtubule branching by microtubule nucleation factor SSNA1. *Nat. Cell Biol.* **20**, 1172–1180.
35. Maeder, C.I., San-Miguel, A., Wu, E.Y., Lu, H., and Shen, K. (2014). In vivo neuron-wide analysis of synaptic vesicle precursor trafficking. *Traffic* **15**, 273–291.
36. Darcy, K.J., Staras, K., Collinson, L.M., and Goda, Y. (2006). Constitutive sharing of recycling synaptic vesicles between presynaptic boutons. *Nat. Neurosci.* **9**, 315–321.
37. Fernandez-Alfonso, T., and Ryan, T.A. (2008). A heterogeneous “resting” pool of synaptic vesicles that is dynamically interchanged across boutons in mammalian CNS synapses. *Brain Cell Biol.* **36**, 87–100.
38. Rizzoli, S.O. (2014). Synaptic vesicle recycling: steps and principles. *EMBO J.* **33**, 788–822.
39. Staras, K., Branco, T., Burden, J.J., Pozo, K., Darcy, K., Marra, V., Ratnayaka, A., and Goda, Y. (2010). A vesicle superpool spans multiple presynaptic terminals in hippocampal neurons. *Neuron* **66**, 37–44.
40. McInnes, J., Wierda, K., Snellinx, A., Bounti, L., Wang, Y.C., Stancu, I.C., Apostolo, N., Gevaert, K., Dewachter, I., Spiess-Jones, T.L., et al. (2018). Synaptogyrin-3 mediates presynaptic dysfunction induced by tau. *Neuron* **97**, 823–835.e828.
41. Zhou, L., McInnes, J., Wierda, K., Holt, M., Herrmann, A.G., Jackson, R.J., Wang, Y.C., Swerts, J., Beyens, J., Miskiewicz, K., et al. (2017). Tau association with synaptic vesicles causes presynaptic dysfunction. *Nat. Commun.* **8**, 15295.
42. Sherwood, N.T., Sun, Q., Xue, M., Zhang, B., and Zinn, K. (2004). *Drosophila* spastin regulates synaptic microtubule networks and is required for normal motor function. *PLoS Biol.* **2**, e429.
43. Trotta, N., Orso, G., Rossetto, M.G., Daga, A., and Broadie, K. (2004). The hereditary spastic paraplegia gene, spastin, regulates microtubule stability to modulate synaptic structure and function. *Curr. Biol.* **14**, 1135–1147.
44. Bodaleo, F.J., and Gonzalez-Billault, C. (2016). The presynaptic microtubule cytoskeleton in physiological and pathological conditions: lessons from *drosophila* Fragile X Syndrome and hereditary spastic paraplegias. *Front. Mol. Neurosci.* **9**, 60.
45. Lu, R., Wang, H., Liang, Z., Ku, L., O’donnell, W.T., Li, W., Warren, S.T., and Feng, Y. (2004). The fragile X protein controls microtubule-associated protein 1B translation and microtubule stability in brain neuron development. *Proc. Natl. Acad. Sci. USA* **101**, 15201–15206.
46. Zhang, Y.Q., Bailey, A.M., Matthies, H.J., Renden, R.B., Smith, M.A., Speese, S.D., Rubin, G.M., and Broadie, K. (2001). *Drosophila* fragile X-related gene regulates the MAP1B homolog Futsch to control synaptic structure and function. *Cell* **107**, 591–603.

47. Liu, J., Pasini, S., Shelanski, M.L., and Greene, L.A. (2014). Activating transcription factor 4 (ATF4) modulates post-synaptic development and dendritic spine morphology. *Front. Cell. Neurosci.* 8, 177.
48. Stepanova, T., Smal, I., van Haren, J., Akinci, U., Liu, Z., Miedema, M., Limpens, R., van Ham, M., van der Reijden, M., Poot, R., et al. (2010). History-dependent catastrophes regulate axonal microtubule behavior. *Curr. Biol.* 20, 1023–1028.
49. dal Maschio, M., Ghezzi, D., Bony, G., Alabastri, A., Deidda, G., Brondi, M., Sato, S.S., Zaccaria, R.P., Di Fabrizio, E., Ratto, G.M., and Cancedda, L. (2012). High-performance and site-directed in utero electroporation by a triple-electrode probe. *Nat. Commun.* 3, 960.

## STAR★METHODS

## KEY RESOURCES TABLE

REAGENT or RESOURCE	SOURCE	IDENTIFIER
Chemicals and reagents		
D-AP5	Tocris	0106
CNQX	Tocris	0190
Bicuculline	Sigma Aldrich	14343
Ammonium Chloride	Sigma Aldrich	254134
BDNF	R&D Systems	248-BDB
Lipofectamine 2000	ThermoFisher	11668019
Neurobasal	ThermoFisher	1103049
B-27 Supplement (50X)	ThermoFisher	7504044
GlutaMAX Supplement	ThermoFisher	35050061
Penicillin-Streptomycin	ThermoFisher	15140163
Trypsin 0.05% EDTA	ThermoFisher	25300054
10x HBSS	ThermoFisher	14065056
NuPAGE MOPS SDS Running buffer	ThermoFisher	NP0001
NuPAGE Antioxidant	ThermoFisher	NP0005
Fluoromount-G	Southern Biotech	0100-01
32% PFA	Electron Microscopy Sciences	15714-S
50% glutaraldehyde	Electron Microscopy Sciences	16300
Poly-D-Lysine	Sigma Aldrich	P1149
Fetal bovine serum	HyClone	SH30071.03
Bovine serum albumin (BSA)	Sigma Aldrich	A9418
DTT	GoldBio	DTT
NuPAGE antioxidant	ThermoFisher	NP0005
NuPAGE MOPS SDS running buffer	ThermoFisher	NP0001
Critical Commercial Assays		
PureLink HiPure Plasmid Maxiprep Kit	ThermoFisher	K210007
Bacteria strains		
DH5a	New England BioLabs	C29871
XL1-Blue	Agilent	200229
Recombinant DNA		
EB3-EGFP	Gift from Franck Polleux	N/A
Mito-DsRed2	Gift from Franck Polleux	N/A
Synaptophysin-Venus	Gift from Franck Polleux	N/A
vGlut1-mTagBFP2	Gift from Franck Polleux	N/A
pCMV-GCaMP7s	Gift from Inbal Israely [32]	N/A
vGlut1-pHluorin	Gift from Clarissa Waites	N/A
vGlut1-mCherry	Gift from Clarissa Waites	N/A
VAMP2-mCherry	Gift from Clarissa Waites	N/A
Rab5-EGFP	Gift from Clarissa Waites	N/A
EGFP-Rab7a	Gift from Richard Vallee	N/A
LAMP1-EGFP	Gift from Volker Haucke [31]	N/A
ARI8b-EGFP	Gift from Volker Haucke [31]	N/A
Gamma-tubulin-mEmerald	Addgene	54105
mEmerald-N1	Addgene	53976

(Continued on next page)

**Continued**

REAGENT or RESOURCE	SOURCE	IDENTIFIER
pLKO.1 sh $\gamma$ -tubulin #1	Sigma Aldrich	TRCN0000089905
pLKO.1 sh $\gamma$ -tubulin #2	Sigma Aldrich	TRCN0000089907
pLKO.1 shHAUS1	Sigma Aldrich	TRCN0000192324
pLKO.1 shHAUS7	Sigma Aldrich	TRCN0000345686
<b>Antibodies</b>		
Mouse $\gamma$ tubulin (TU-30)	Exbio	11-465; RRID: AB_10735452
Mouse GAPDH	Abcam	Ab8245; RRID: AB_2107448
Rabbit GAPDH	ThermoFisher	PA1-987; RRID: AB_2107311
Rabbit HAUS1	ThermoFisher	PA5-59218; RRID: AB_2642315
Mouse HAUS7	ThermoFisher	MA5-26313; RRID: AB_2724420
Mouse acetylated tubulin	Sigma Aldrich	T6793; RRID: AB_477585
Rabbit $\beta$ III-tubulin	Abcam	Ab18207; RRID: AB_444319
Rabbit synapsin1	SYSY	106011; RRID: AB_2619772
Mouse synapsin 1	SYSY	106003; RRID: AB_2619773
Goat anti-mouse IgG (H+L) Highly Cross-adsorbed Secondary Antibody, Alexa Fluor 488-conjugated	ThermoFisher	A11029; RRID: AB_138404
Goat anti-rabbit IgG (H+L) Highly Cross-adsorbed Secondary Antibody, Alexa Fluor 488-conjugated	ThermoFisher	A11034; RRID: AB_2576217
Goat anti-mouse IgG (H+L) Highly Cross-adsorbed Secondary Antibody, Alexa Fluor 546-conjugated	ThermoFisher	A11030; RRID: AB_144695
Goat anti-rabbit IgG (H+L) Highly Cross-adsorbed Secondary Antibody, Alexa Fluor 546-conjugated	ThermoFisher	A11035; RRID: AB_143051
IRDye® 680RD Goat anti-Mouse IgG Secondary Antibody	LI-COR	926-68070; RRID: AB_10956588
IRDye® 800CW Goat anti-Rabbit IgG Secondary Antibody	LI-COR	926-32211; RRID: AB_621843
<b>Experimental Models: Organisms/Strains</b>		
Mouse: C57BL/6J	Charles River Laboratories	RRID:IMSR_CRL:027
Rat: Sprague Dawley	Charles River Laboratories	RRID:RGD_734476
<b>Software</b>		
ImageJ (Fiji)	NIH	RRID: SCR_002285
GraphPad Prism	GraphPad	RRID: SCR_002798
MetaMorph Microscopy Automation and Image Analysis Software	Molecular Devices	RRID: SCR_002368
LI-COR Image Studio Software	LI-COR	RRID:SCR_015795
Zeiss ZEN	Zeiss	RRID:SCR_013672
Andor iQ3	Oxford Instruments	RRID:SCR_014461
<b>Other</b>		
35mm MatTek dishes	MatTek	P35G-1.5-14-C
NuPAGE Gel	ThermoFisher	NP0316
Nitrocellulose membrane	Fisher	10600011
18mm No.1 circle coverglass	Carolina	633033
22mm No.1 square coverglass	Carolina	633035

**LEAD CONTACT AND MATERIALS AVAILABILITY**

Further information and requests for resources and reagents should be directed to and will be fulfilled by the Lead Contact, Francesca Bartolini ([fb2131@columbia.edu](mailto:fb2131@columbia.edu)). Plasmids generated in this paper will be available upon request.

**EXPERIMENTAL MODEL AND SUBJECT DETAILS**

All protocols and procedures for rats and mice were approved by the Committee on the Ethics of Animal Experiments of Columbia University and according to Guide for the Care and Use of Laboratory Animals of the National Institutes of Health. Time-pregnant

Sprague Dawley rats (Embryonic Day 18) were purchased from Charles River Laboratories for primary hippocampal neuronal cultures. Timed-pregnant female mice were obtained by mating C57BL/6J mice from Charles River Laboratories in house. At the time of *in utero* electroporation (Embryonic Day 15.5), littermates were randomly assigned to experimental groups without regard to their sex. Electroporated mice were born and group housed with the mother until weaning under standard laboratory conditions with food and water *ad libitum* and maintained in a 12 h light/dark cycle. Mice were sacrificed at 21–28 days old for acute hippocampal slices.

### Primary hippocampal neuronal cultures

Primary hippocampal neuronal cultures were prepared as previously described [47]. Briefly, hippocampi were dissected from E18 rats, and neurons plated on 100  $\mu\text{g}/\text{mL}$  poly-D-lysine-coated 12-well-plates at the density of  $3 \times 10^5$  cells/well for biochemistry assays,  $5 \times 10^4$  cells/dish for live imaging in the chamber of 35 mm MatTek dishes, or  $4 \times 10^4$  cells/cover slip on 18 mm coverslips for immunofluorescence. Primary neurons were maintained in Neurobasal medium (Invitrogen) with the supplement of 2% B-27 (Invitrogen) and 0.5 mM glutamine (Invitrogen) at 37°C, and 1/3 of the medium was changed every 3–4 days up to 3 weeks in culture.

### Acute hippocampal slices

Acute hippocampal slices (200  $\mu\text{m}$ ) were prepared from 21–28 days old electroporated mice using a vibratome (Leica Biosystem VT 1000S) and collected in complete HBSS media (HBSS, 30 mM glucose, 1 mM  $\text{CaCl}_2$ , 1 mM  $\text{MgSO}_4$ , 4 mM  $\text{NaHCO}_3$ , and 2.5 mM HEPES, pH 7.4). Acute slices were immediately transferred in 35 mm MatTek dishes for live imaging.

## METHOD DETAILS

### Lentiviral shRNA silencing

Production of lentiviral particles was conducted using the 2<sup>nd</sup> generation packaging system as previously described [47]. Briefly, HEK293T were co-transfected with lentiviral shRNA constructs and the packaging vectors pLP1, pLP2, and pLP-VSV-G (Invitrogen) using calcium phosphate. 48 h and 72 h after transfection, the virus was collected, filtered through 0.22  $\mu\text{m}$  filter, and further concentrated by ultracentrifugation. Concentrated virus was aliquoted and stored at  $-80^\circ\text{C}$ .

Lentiviral constructs to knockdown  $\gamma$ -tubulin were purchased from Sigma Aldrich (TRCN000089905 and TRCN000089907) with the following DNA sequence 5'- CCGGGCAATCAGATTGGGTTTCGAGTCTCGAGACTCGAACCCAATCTGATTGCTTTTTTG-3' and 5'-CCGGGCAGCAGCTGATTGACGAGTACTCGAGTACTCGTCAATCAGCTGCTGCTTTTTTG-3'

onto pLKO.1 lentivector. Lentiviral constructs to knockdown HAUS1 and HAUS7 were purchased from Sigma Aldrich (TRCN0000192324 and TRCN0000345686) with the following DNA sequence 5'- CCGGCTTCTCATGGAGAGTGTGAACCTCGAGTTCACACTCTCCATGAGAAAGTTTTTG-3' and 5'-

CCGGCCAGATGACCAGGATCTTCTACTCGAGTAGAAGATCCTGGTCATCTGGTTTTTG-3' onto pLKO.1 lentivector. The pLKO.1 vector with noncoding (NC) sequence was used as control.

### Western blot analyses

Cells were lysed in Laemmli sample buffer and boiled at 96°C for 5 min. Cell lysates were sonicated by a probe sonicator to shear cellular debris and genomic DNA. To detect tubulins, lysates were diluted 1:10 in sample buffer. Proteins were separated by 10% Bis-Tris gel (Invitrogen) and transferred onto nitrocellulose membrane. After blocking in 5% milk/TBS or BSA/TBS, membranes were incubated with primary antibodies at 4°C overnight prior to 1 h incubation with secondary antibodies. Image acquisition was performed with an Odyssey imaging system (LI-COR Biosciences, NE) and analyzed with Odyssey software.

### Immunofluorescence microscopy and analyses

For MT staining, neurons were fixed in 3.7% PFA, 0.25% glutaraldehyde, 3.7% sucrose and 0.1% Triton X-100 for 15 min and quenched in 1 mg/mL sodium borohydride/PBS. For  $\gamma$ -tubulin, HAUS7, GAPDH and synapsin staining, neurons were fixed in 4% PFA for 15 min. Cells were then washed in PBS, blocked in 2% FBS, 2% BSA, and 0.2% fish gelatin in PBS for 1 h, and stained with primary antibodies for 2 h followed by secondary antibodies for 1 h. Mounted samples were observed by a Zeiss LSM 800 confocal microscope equipped with Airyscan module, using a 63x objective (Plan-Apochromat, NA 1.4). Images were obtained and processed for super resolution using Zen Blue 2.1 software. All images were analyzed by ImageJ software except for pseudo-color presentation of vGlut-pHluorin experiments that were instead obtained using Metamorph software.

### Live imaging of MT, organelle and SV dynamics

Neurons grown on MatTek dishes were co-transfected with EB3-EGFP or EB3-tdTomato using Lipofectamine 2000 (Invitrogen), together with presynaptic markers vGlut1-mCherry, vGlut1-Venus, vGlut1-mTagBFP2, or VAMP2-mCherry. For organelle dynamics, triple transfection of EB3, vGlut1, together with the organelle markers Rab5-EGFP, EGFP-Rab7a, LAMP1-GFP, or mitoDsRed were performed using Lipofectamine 2000. Live cell imaging was performed 24–48 h after transfection in complete HBSS media (HBSS, 30 mM glucose, 1 mM  $\text{CaCl}_2$ , 1 mM  $\text{MgSO}_4$ , 4 mM  $\text{NaHCO}_3$ , and 2.5 mM HEPES, pH 7.4) using IX83 Andor Revolution XD Spinning Disk Confocal System. The microscope was equipped with a 100  $\times$  /1.49 oil UApO objective, a multi-axis stage controller (ASI MS-2000), and a controlled temperature and  $\text{CO}_2$  incubator. Movies were acquired with an Andor iXon Ultra EMCCD camera and Andor iQ 3.6.2

live cell imaging software at 0.5–2 s/frame for 3 min. For pharmacological induction of neuronal activity, neurons were pretreated with 50  $\mu\text{M}$  D-AP5 for 6–12 h prior to live imaging in complete neurobasal media, then changed to complete HBSS media with the same concentration of D-AP5 for live imaging. To induce neuronal activity, neurons were washed 3x with complete HBSS media and 20  $\mu\text{M}$  bicuculline or DMSO control was added to complete HBSS media after washes. For BDNF induction of neuronal activity, 50 ng/mL BDNF was directly added to complete HBSS media during live imaging. Movies were taken 1 min upon treatment. Maximum projections of movies were performed by Image Math within Andor software, exported as Tiff files and analyzed in ImageJ. Kymographs were generated by drawing a region from the proximal to the distal axons (within 100  $\mu\text{m}$  from the cell body) based on morphology and anterograde movement of EB3-labeled comets. Presynaptic MTs were classified based on their plus end contacts with stable vGlut1 or VAMP2 labeled boutons. In our measurements of EB3 tracks starting or ending at boutons, we also included those that start or end at a bouton and pass through the next distal or proximal boutons. Parameters describing MT dynamics were defined as follows: rescue/nucleation frequency: number of rescue or nucleation events per  $\mu\text{m}^2$  per min; catastrophe frequency: number of full tracks/total duration of growth; comet density: number of comets per  $\mu\text{m}^2$  per min; growth length: comet movement length in  $\mu\text{m}$ ; comet lifetime: duration of growth; growth rate: growth length/comet lifetime [48]. Parameters describing organelle and SV dynamics were defined as follows: % of moving puncta: number of moving puncta/number of total puncta x 100; % of tracks start/end at boutons: number of tracks start or end at boutons/number of total moving tracks x 100; % of retrograde tracks: number of retrograde tracks/number of total moving tracks x 100.

### **In utero electroporation and live-imaging of acute hippocampal slices**

A mix of endotoxin-free plasmid EB3-EGFP (1.5 mg/mL) and vGlut-mCherry (1.2 mg/mL) and 0.5% Fast Green (Sigma) was injected into one lateral hemisphere of E15.5 embryos using a Picospritzer III (Parker). Electroporation (ECM 830, BTX) was performed with 5 mm electrode tweezers (Nepagene, Japan) to target hippocampal progenitors in E15.5 embryos using a triple electrode setup according to dal Maschio et al. [49]. Five pulses of 45 V for 50 ms with 500 ms intervals were used for electroporation. Animals were sacrificed 21–28 days after birth. Acute hippocampal slices were prepared as in experimental model and subject details section. Electroporated hippocampal neurons from CA1 region were selected and imaged using an inverted Nikon Ti-E microscope with Nikon Elements Software at 37°C. 488 and 561 nm lasers were used as light source and shuttered by Acousto-Optic Tunable Filters (AOTF). Live-imaging acquisition of EB3 comets relative to vGlut1 positive stable puncta within 50–100  $\mu\text{m}$  of cell bodies was performed for 300 s using a 60x oil-immersion objective (NA1.4) at 3 s/frame.

### **Live imaging of SV exo-/endocytosis**

To test synaptic exo-endocytosis via the vGlut-pHluorin assay using electrical field stimulation, hippocampal neurons were infected with noncoding shNC control or two independent shRNAs against  $\gamma$ -tubulin (sh $\gamma$ -tub #1 or #2) lentiviruses at 12DIV and co-transfected with vGlut-pHluorin and mCherry at 13DIV. Imaging of live neurons was performed at 16DIV in Tyrode's buffer containing 119 mM NaCl, 2.5 mM KCl, 2 mM  $\text{MgCl}_2$ , 2 mM  $\text{CaCl}_2$ , 25 mM HEPES, pH 7.4, 30 mM D-glucose, 10  $\mu\text{M}$  6-cyano-7-nitroquinoxaline-2,3-dione (CNQX; Tocris), and 50  $\mu\text{M}$  D-(-)-2-amino-5-phosphonopentanoic (D-AP5 or APV; Tocris) buffered to pH 7.4 at 37°C. Images were acquired with a 40X objective (Neofluar, NA 1.3) on an epifluorescence microscope (Axio Observer Z1, Zeiss) with Colibri LED light source, EMCCD camera (Hamamatsu) and Zeiss Zen software. Stills of the mCherry and pHluorin channels were acquired followed by a 300 s time lapse of the pHluorin channel recorded at 5 s/frame. Action potentials (AP) were evoked by passing 1 msec bipolar current through platinum-iridium electrodes connected to metal tubes containing imaging buffer at 10 Hz using a digital stimulator (World Precision Instruments) and a stimulator isolator (World Precision Instruments). Tyrode's buffer supplemented with 50 mM  $\text{NH}_4\text{Cl}$  was perfused at the end of the recording to assess maximum pHluorin signal.

### **Live imaging of $\text{Ca}^{2+}$ influx by GCaMP7s**

Primary hippocampal neurons (16DIV) were infected with noncoding shNC control or two independent shRNAs against  $\gamma$ -tubulin (sh $\gamma$ -tub #1 or #2) lentiviruses at 12DIV and co-transfected with GCaMP7s and vGlut1-mCherry at 13DIV. Live imaging was performed at 16DIV using the same microscopy setup and protocol as SV exo-/endocytosis without  $\text{NH}_4\text{Cl}$  dequenching at the end of each recording.

## **QUANTIFICATION AND STATISTICAL ANALYSIS**

Data are shown as means  $\pm$  SEMs from at least 3 independent experiments and figures are generated by GraphPad Prism. Image analysis was performed by ImageJ (Fiji), MetaMorph Image Analysis Software, Zeiss Zen, and Andor iQ3. Western blot analysis was performed by LI-COR Image Studio Software. Statistical analysis between two groups was performed using Student's t tests ( $N > 15$ ), Mann-Whitney tests (unpaired samples  $N < 15$  in [Figures S1A and S1B](#); [Figure 2C](#); [Figures S2B, S2D, S2G, and S2J](#); [Figure 3](#)

comparing untreated and AP5 washout with bicuculline; [Figure S3](#) comparing untreated and AP5 washout with bicuculline; [Figure 4](#); [Figures S4D–S4J](#)), or Wilcoxon matched-pairs signed rank test (paired samples  $N < 15$  in [Figures 1B, 1C, 1F, 1H, and 1J](#); [Figures S1D, S1E, S1F, and S1H](#); [Figure 2H](#); [Figure 3](#) comparing before and after AP5 washout with bicuculline or before and after BDNF treatment; [Figure S3](#) comparing before and after AP5 washout with bicuculline). Comparison among 3 or more groups was performed using the Kruskal-Wallis test with Dunn's multiple comparisons test for non-parametric unpaired one way ANOVA (unpaired samples  $N < 15$  in [Figures 2D, 2F, 2G, 2J, and 2K](#); [Figures S2H and S2L](#); [Figures S4A–S4C](#)). Statistical significance was set for  $p < 0.05$ .

#### **DATA AND CODE AVAILABILITY**

The published article includes all data generated or analyzed during this study.